Journal of Biomedical Optics

BiomedicalOptics.SPIEDigitalLibrary.org

Contact, high-resolution spatial diffuse reflectance imaging system for skin condition diagnosis

Nils Petitdidier
Anne Koenig
Rémi Gerbelot
Henri Grateau
Sylvain Gioux
Pierre Jallon

SPIE.

Nils Petitdidier, Anne Koenig, Rémi Gerbelot, Henri Grateau, Sylvain Gioux, Pierre Jallon, "Contact, high-resolution spatial diffuse reflectance imaging system for skin condition diagnosis," *J. Biomed. Opt.* **23**(11), 115003 (2018), doi: 10.1117/1.JBO.23.11.115003.

Contact, high-resolution spatial diffuse reflectance imaging system for skin condition diagnosis

Nils Petitdidier,[a,b,c,*] Anne Koenig,[a] Rémi Gerbelot,[a] Henri Grateau,[a] Sylvain Gioux,[b,c] and Pierre Jallon[a]
[a]Université Grenoble Alpes, Grenoble, France
[b]Laboratoire ICube, Télécom Physique Strasbourg, Illkirch, France
[c]Université de Strasbourg, Strasbourg, France

Abstract. Spatially resolved diffuse reflectance spectroscopy (srDRS) is a well-established technique for noninvasive, *in vivo* characterization of tissue optical properties toward diagnostic applications. srDRS has a potential for depth-resolved analysis of tissue, which is desired in various clinical situations. However, current fiber-based and photodiode-based systems have difficulties achieving this goal due to challenges in sampling the reflectance with a high enough resolution. We introduce a compact, low-cost architecture for srDRS based on the use of a multipixel imaging sensor and light-emitting diodes to achieve lensless diffuse reflectance imaging in contact with the tissue with high spatial resolution. For proof-of-concept, a prototype device, involving a commercially available complementary metal–oxide semiconductor coupled with a fiber-optic plate, was fabricated. Diffuse reflectance profiles were acquired at 645 nm at source-to-detector separations ranging from 480 μm to 4 mm with a resolution of 16.7 μm. Absorption coefficients (μ_a) and reduced scattering coefficients (μ_s') of homogeneous tissue-mimicking phantoms were measured with $4.2 \pm 3.5\%$ and $7.0 \pm 4.6\%$ error, respectively. The results obtained confirm the potential of our approach for quantitative characterization of tissue optical properties in contact imaging modality. This study is a first step toward the development of low-cost, wearable devices for skin condition diagnosis *in vivo*. *© 2018 Society of Photo-Optical Instrumentation Engineers (SPIE)* [DOI: 10.1117/1.JBO.23.11.115003]

Keywords: diffuse reflectance; tissue spectroscopy; optical properties; contact imaging; CMOS sensor; wearable device.

Paper 180306R received May 31, 2018; accepted for publication Oct. 15, 2018; published online Nov. 13, 2018.

1 Introduction

Diffuse reflectance spectroscopy (DRS) has been widely used to determine absorption and scattering properties of turbid media. When applied to biological tissue such as skin, DRS provides quantitative characterization of tissue composition for diagnostic purposes. The reduced scattering coefficient (μ_s') is sensitive to cells and tissue morphology, while the absorption coefficient (μ_a) relates to the biochemical content of tissue and may be used to infer the concentration of particular molecular species. In the visible and near-infrared domain, these notably include oxyhemoglobin, deoxyhemoglobin, melanin, and bilirubin, which are of great interest in a variety of clinical situations. Many groups have investigated DRS as a noninvasive tool to provide diagnostic criteria *in vivo*. Examples of application include tissue oxygenation monitoring,[1–3] tumor margin assessment in epithelium,[4,5] breast and colon cancer detection,[6,7] jaundice diagnosis in new-born skin,[8] pharmacokinetics,[9] or port-wine stain treatment evaluation.[10]

Spatially resolved diffuse reflectance spectroscopy (srDRS) is a particular implementation of DRS that consists of analyzing the spatial dependence of diffuse reflectance profiles produced by a given arrangement of light sources and detectors. By exploiting the spatially dependent influence of optical parameters on the diffuse reflectance intensity, determination of absorption and scattering parameters can be achieved. Furthermore, the measurement of photons at multiple source-to-detector separations (SDS) provides a potential for depth-resolved analysis.[11] Translation of srDRS into the clinic necessitates an optimized combination of sources and detectors, as well as modeling of light transport in tissue and specific constraints related to the targeted application.

Various ways to implement srDRS have been reported in the literature.[1,5,12–16] Most common srDRS instruments involve a broadband source and a spectrophotometer, both coupled to a fiber-optic probe ensuring light delivery and collection directly in contact with tissue. This approach has led to the development of portable instruments that have been deployed in a variety of clinical and preclinical studies.[5,16,17] Typical fiber-based probes consist of a concentric arrangement of multiple collection fibers around a central illumination fiber for maximization of signal-to-noise ratio (SNR),[5,16] as shown in Fig. 1(a). However, the fill factor and light collection efficiency of the system are limited by the density of the fibers as well as the cladding and low numerical aperture (NA) of the fibers. As a result, typically less than 10 source-to-detector separations (SDS) can be used, limiting the ability of the instrument to achieve depth specific analysis of tissue.

Recently, alternative approaches have been investigated for further miniaturization of srDRS devices. Several groups used photodiodes (PD) in contact with tissue to collect the diffuse reflectance.[18,19] The higher NA of PDs compared to optical fibers improved light collection efficiency. However, instruments reported in these studies only involved single PD–source pairs and thus did not exploit the spatial profile of diffuse reflectance spectra. Later, this issue was addressed by

*Address all correspondence to: Nils Petitdidier, E-mail: nils.petitdidier@etu.unistra.fr

1083-3668/2018/$25.00 © 2018 SPIE

Senlik and Jokerst, who developed a custom probe made of an array of multiple concentric annular PDs surrounding a central illumination aperture.[14] Spatially resolved diffuse reflectance spectra were acquired at 24 SDS ranging from 400 to 3550 μm. Such approach may have significant potential for the analysis of layered tissue using a wearable system. However, such solution involves the development of custom PD arrays, and the detection of spatially resolved diffuse reflectance is restricted to a particular geometry.

Alternatively, scattered light from tissue may be detected at a high resolution using a multipixel image sensor, typically a charge-coupled device (CCD) or a complementary metal–oxide semiconductor (CMOS) sensor. This approach was followed by several groups, who used camera-based systems to analyze the spatial dependence of diffuse reflectance spectra, either in real-space[13] or frequency-domain.[2,3] Because of the high number of considered SDS, such systems may have significant potential to achieve depth-specific analysis of layered tissue such as skin and cervix, leading to important diagnostic criteria.[3,20,21] However, focusing optics are usually employed for remote collection of scattered photons, thereby increasing the cost and complexity of the device.

Recently, the removal of the focusing optics to achieve high-resolution imaging of scattered light from turbid samples using a contact geometry has been investigated.[22–24] Notably, Schelkanova et al.[23] employed a color CMOS sensor directly coupled to silicon phantoms and combined with a broadband source. Using this system, the authors were able to visualize subsurface microfluidic patterns mimicking epithelial vascular structures. Yet, quantitative characterization of optical parameters was not intended considering the broad bandwidth of the CMOS RGB channels.

In this work, we investigate the use of a standard high-resolution multipixel image sensor to achieve quantitative characterization of tissue optical properties in contact modality [see Fig. 1(b)]. Commercial imaging sensors based on the CMOS technology are readily available at low cost and with constantly improving optical and electronical performance. We believe that there is opportunity to exploit this technology to address a new range of clinical situations requiring cost-effective, tightly packed tissue characterization tools. In order to evaluate the potential of our approach, a prototype instrument was designed and fabricated. The instrument is made of a commercially available CMOS sensor combined with a dedicated fiber-based coupling system. The coupling system employs a surface mounted light-emitting diode (LED) and a fiber-optic plate (FOP), ensuring efficient photons transfer onto the CMOS pixel array at high spatial resolution, thereby overcoming the limitations of current fiber-based and PD-based systems. In this paper, we describe the design of the instrument, introduce the developed prototype, and finally evaluate the prototype performance on tissue-mimicking optical phantoms.

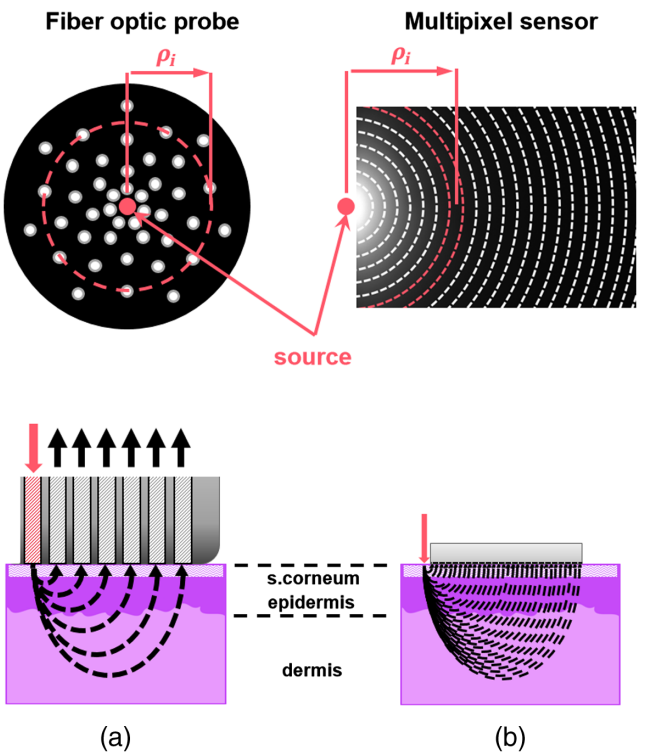

Fig. 1 Detection schemes for (a) fiber-based and (b) CMOS-based srDRS instruments. Views from the top (top) and side (bottom) of the instruments are provided. The diffuse reflectance at distance ρ_i to the source is radially averaged (red-dotted lines).

2 Materials and Methods

2.1 *Light Sensor*

In order to sample the diffuse reflectance from turbid media with high spatial resolution, we employed an eight-bit monochrome CMOS camera purchased from IDS Imaging Inc. (UI-1492-LE-M). This sensor had a 6.413×4.589 mm^2 active area with 1.67-μm pixel pitch. The relatively low dynamic range of detection was compensated by the use of a dynamic expansion procedure, which is detailed in Sec. 2.3.3. In the next paragraph, we describe the dedicated coupling system that was developed to produce and collect diffuse reflectance patterns in contact imaging modality. A layout of the sensor and coupling system architectures is shown in Fig. 2.

2.2 *srDRS Coupling System*

In the architecture considered in our study, the light emitter and receiver are positioned next to one another, in contact with the analyzed medium. The most intuitive approach is to place

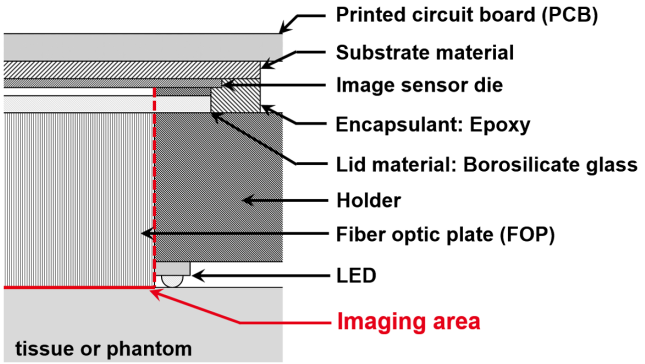

Fig. 2 Layout of the CMOS-based contact imaging system for srDRS. The imaging area (red line) is transported from the CMOS pixel area to the bottom face of the fiber optic plate, which is placed in contact with the analyzed sample.

the CMOS sensor itself in contact with tissue to both collect and detect scattered photons, as proposed in Ref. 23. In such configuration, the presence of wire bonds and protective encapsulant on every sides of the sensitive area prohibits the placement of a light source in close proximity to the sensor. Several studies have pointed out that spatially resolved diffuse reflectance from tissue was most sensitive to μ_s' at short distances to the illumination point, typically below 1 mm, while being both dependent on μ_a and μ_s' further away from the source.[11,25] As a consequence, access to both short and large SDS is needed for accurate determination of absorption and scattering parameters. The packaging of commercial CMOS sensors thus constitutes a clear limitation toward the implementation of a performing srDRS device.

In order to overcome this limitation, we propose to insert an FOP between the sensor and the analyzed medium. FOPs are formed by a network of micron-sized optical fibers densely packed into a glass or polymer material that performs image transfer between the top and bottom faces of the plate. FOPs can support high-resolution imaging up to 160 lp/mm and exceed 60% in diffused light transmittance.[26] They can be purchased with various shapes, NA and can be tapered to achieve magnification/demagnification.

FOP-coupled CMOS/CCD imaging platforms are involved in both scientific and industrial applications, including x-ray imaging,[27] biosensing,[28] display screen enhancement, and fingerprint reading.[26] In recent work, Schelkanova et al.[24] evaluated the applicability of this architecture for diffuse reflectance imaging. The authors emulated a 2-D fiber-optic grid by a single fiber scanning system for visualization of subsurface patterns in turbid phantoms. However, quantification of absorption and scattering parameters was not investigated.

In this case, insertion of an FOP can be exploited to provide access to short SDS. Dimensions and positioning of the FOP can be optimized to produce a 1:1 image conjugation between the CMOS-sensitive area and the surface of tissue delimited by the FOP edges. In this manner, borders of the imaging area become physically accessible. The FOP thickness can be adapted to insert a light source between the CMOS chip and tissue, at the closest possible distance to the first detection point. For example, LEDs may be employed to generate the desired diffuse reflectance signals. LEDs are available at many wavelengths, can be highly miniaturized, and are inexpensive, which may participate in the reduction of srDRS systems footprint and cost.

For this study, a custom FOP with 6-μm unit fiber core diameter (OS-ST, SZPhoton) was purchased.[26] The FOP was positioned to ensure alignment of the pixel area borders with FOP edges on one side, against which an LED (KPTD-1608SURCK, Kingbright) emitting at 645 nm was mounted. The top of the LED dome lens was placed to be coplanar with the collection face of the FOP. In this configuration, the LED chip was separated by a distance of 480 μm to the FOP edge. From the technical information provided by the manufacturer, the number of individual fibers in front of the imaging area was estimated to 1.308×10^5. The FOP and LED were held in a 30-mm Thorlabs (Thorlabs Inc., Newton, New Jersey) cage due to a homemade dedicated element. Optical grease was used for index matching optimization between the FOP and the CMOS protective glass lid. Finally, silicon treatment was performed to ensure isolation and impermeability of the exposed electronic parts of the device.

2.3 *Experiments*

2.3.1 *Optical phantoms*

In order to evaluate the potential of the developed system for the characterization of absorption and scattering properties of tissue, validation experiments were conducted on homogeneous liquid phantoms, following a methodology employed by other authors.[13,15,29] Phantoms consisted of solutions of 20% Intralipid fat and black India ink (Rotring Inc., Hamburg, Germany) at varying concentrations in distilled water. The absorbance A of solutions was measured by a spectrophotometer (CARY 300, Agilent) in a 1-cm tank, yielding the absorption coefficient $\mu_a = \ln(10) \times A$. Then, various quantities of intralipid fat were added to generate scattering in the medium. Note that the dilution of the ink due to the addition of Intralipid was taken into account in the determination of phantom absorption coefficients. For this, we applied the following dilution factor: $F = 1 - P/20$, where P is the percentage of Intralipid in the phantom, to the absorption coefficient derived from the absorbance measurements.

Based on the work of Van Staveren et al.,[30] the following equations were derived to calculate the anisotropy factor g and scattering coefficient μ_s of phantoms:

$$g(\lambda) = 1.1 - 0.58 \times 10^{-3}\lambda, \tag{1}$$

$$\mu_s(\lambda) = 2.54 \times 10^9 \lambda^{-2.4} \times P/10, \tag{2}$$

where λ is in nanometers and μ_s is in units of cm^{-1}. The additional $P/10$ factor in Eq. (2) was used to scale the equation of Van Staveren et al. (derived for a 10%-Intralipid solution) to the percentages of Intralipid used in our study.

A set of 15 phantoms, which consisted of three groups of 1%, 2%, and 3% Intralipid concentration, respectively, referred to as IL1%, IL2%, and IL3%, was fabricated. Each group was composed of five phantoms with varying ink concentration. Corresponding reduced scattering and absorption coefficients ranged from 12.7 to 38.1 cm^{-1} and 0.31 to 2.30 cm^{-1}, respectively, spanning values representative of skin properties.[31,32]

2.3.2 *System characterization*

The system linearity was measured by taking the average signal over the whole sensor area at constant illumination level and increasing exposure time. Background subtraction was performed for each exposure time.

For assessment of the source stability, the illumination power out of the LED was monitored over a 1.5-h acquisition period using an optical power meter (PM100D, Thorlabs).

For system noise performance characterization, repeated image acquisitions were made on the least favorable phantom, chosen as the one exhibiting the highest μ_a and μ_s'.

We calculated the SNR {SNR = 20 log[mean intensity/(standard deviation + dark current)]} out of 10 acquisitions for various exposure times. Intensity was averaged over concentric rings surrounding the illumination point, as described in Sec. 2.3.3. The dark current was measured for every exposure by taking the mean signal of dark images over the whole sensor area.

Accurate characterization of optical properties necessitates that the source radial intensity profile be accounted for. The source profile was measured using a CMOS camera (UI-1492-LE-M, IDS Imaging) and a 23-mm objective (Xenoplan 1.4/23-0902,

Schneider Kreusnach). Following the procedure described in Sec. 2.3.3, images were recorded at multiple exposure times and subsequently recombined to measure the radial intensity profile produced by the LED in the plane of the FOP top face with sufficient SNR. Note that the same phantom was used for measurement of the source profile and calibration of the instrument response (see Sec. 2.4.2). The measured profile was then included in the forward model of light propagation (see Sec. 2.4.1).

Finally, flat-field inhomogeneity was corrected by using a Teflon disk with 10 mm thickness. Ten acquisitions were made and averaged. The resulting data were used as normalization factor to correct from spatial heterogeneities in FOP transmission, especially occurring near edges. In order to evaluate the inhomogeneity correction, 10 consecutive measurements of the calibration phantom were made without moving the srDRS device and the standard deviation between pixels on the same ring was compared to the measurement noise (see Sec. 3).

2.3.3 *Acquisition procedure*

Consecutives steps followed during acquisitions are summarized in Fig. 3. For each measurement, reflectance images were recorded with the srDRS device using multiple exposure times. Dark images were taken with the same exposure times and subtracted from reflectance images. The resulting images were then normalized by the corresponding exposure time. This set of dark-subtracted and normalized images was employed to produce a single image, herein referred to as "high dynamic range (HDR) image," using a custom algorithm written in Matlab (Mathworks Inc., Natick, Massachusetts). The HDR image was composed of pixels from images taken at multiple exposure times in a stepwise manner, going from the longest to the shortest exposure. At each step, pixels with values lower than the saturation limit were kept while saturated pixels were discarded and replaced by the corresponding pixels from the next image (i.e., the one recorded with the nearest lower exposure time). We set the saturation limit to 80% of the sensor dynamic so that pixel values in the HDR image remained within the linear behavior of the camera. Note that for each SDS, signals were extracted only from the image providing the best SNR. This procedure (referred to as dynamic expansion in Fig. 3) had to be employed to expand the dynamic range of detection, thereby ensuring sufficient SNR (above 20 dB) up to 4 mm from the source. Depending on phantom properties, three to five different exposure times had to be used. Especially, phantoms with highest absorption and scattering coefficients necessitated additional exposure times compared to phantoms with moderate μ_a and μ_s'. The illumination center was automatically determined through Canny filtering, following a method employed by Foschum et al.[13] Finally, the radial symmetry of illumination was exploited to reduce noise in measured reflectance profiles. Pixel values were averaged over concentric annular areas of 10 pixels thickness around the excitation point. As rings became larger for increasing SDS, a greater number of pixels were used to calculate the reflectance and thereby the SNR drop (for a given exposure time) was slightly mitigated. This step is referred to as ring averaging in Fig. 3.

Following the procedure described before, spatially resolved diffuse reflectance acquisitions were performed on the phantom set. Prior to measurements, phantoms were sonicated for 20 min and left at room temperature for 30 min. During acquisitions, our srDRS device was immersed in phantoms, ~5 mm below the surface. Solutions were regularly stirred to prevent from surface layering of Intralipid.[33] Five measurements were made for each phantom. Between measurements, the system was removed from phantoms and gently cleaned using ethanol and water.

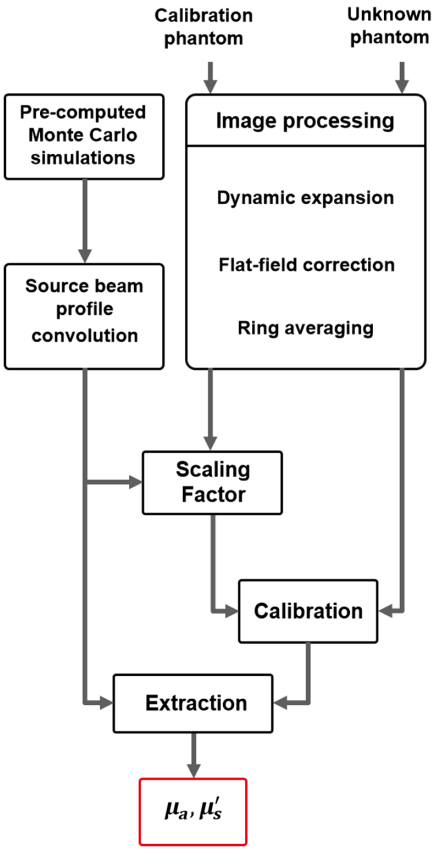

Fig. 3 Flowchart of the data processing steps for optical properties quantification. Raw reflectance images were first recorded (image acquisition). Dark images were then recorded and subtracted from reflectance images (background subtraction). This was done at multiple exposure times. The obtained images were recombined to expand the sensor dynamic (dynamic expansion). Then, pixel values were averaged over concentric annular areas surrounding the illumination center to extract the radial profile of raw diffuse reflectance (ring averaging). Theoretical reflectance profiles were derived from MC simulations and convoluted with the priory measured source beam profile. Measurement of the calibration phantom diffuse reflectance was used to yield a scaling factor through comparison with the theoretical data. The scaling factor was applied to unknown phantoms measurements to convert raw diffuse reflectance profiles into absolute unit. The obtained calibrated reflectance profiles were compared to theoretical data to extract the absorption coefficient (μ_a) and reduced scattering coefficients (μ_s') of phantoms.

The acquisition was controlled using a dedicated LabVIEW interface (National Instruments Inc., Austin, Texas).

2.4 *Data Processing*

A flowchart of data processing steps is shown in Fig. 3. These include description of light propagation in the medium, calibration of the instrument response, and extraction of optical properties through inverse problem solving.

2.4.1 *Forward model*

Theoretical reflectance curves for various optical properties were computed from Monte Carlo (MC) simulations using

a scaling method proposed by Liu and Ramanujam.[34] One million photons were launched in each simulation. A collimated pencil beam vertically incident on a semi-infinite medium with homogeneous optical properties was assumed. We considered a semi-infinite model since phantoms used in this study had homogeneous properties and both depth and width larger than 5 cm. The Henyey–Greenstein phase function was used to calculate photon trajectories after scattering events.[35] Following an approach used in previous studies,[13] simulated reflectance curves were convolved with the measured source beam profile using Matlab.

The obtained reflectance data were stored in a look-up table (LUT). Absorption coefficient values were sampled between 0 and 5 cm^{-1} with 0.02 cm^{-1} step size, while scattering coefficients μ_s ranged from 1 to 300 cm^{-1} with 1 cm^{-1} step size (with $g = 0.724$, equivalent to 0.276 to 82.8 cm^{-1} with 0.276-cm^{-1} step size in reduced scattering coefficient μ_s'). The anisotropy factor g was equal to 0.724, as predicted from Mie theory calculations,[30] for all simulations.

2.4.2 *Calibration*

Calibration of the instrument response must be performed to scale the measured reflectance profiles to MC simulations. Spatially resolved diffuse reflectance measurements were performed on a liquid phantom with known optical properties, herein referred to as calibration phantom. We selected the phantom with lowest absorption and medium scattering level among the available phantom set, accordingly with guidelines previously provided by Bender et al.[36] Following an approach used by other authors,[12,15] the following spatially dependent scaling factor was derived:

$$\mathrm{SF}(\rho) = R_{\mathrm{th}}(\mu_a^{\mathrm{calib}}, \mu_s'^{\mathrm{calib}}, \rho)/R_{\mathrm{meas}}^{\mathrm{calib}}(\rho), \tag{3}$$

where $R_{\mathrm{th}}(\mu_a^{\mathrm{calib}}, \mu_s'^{\mathrm{calib}}, \rho)$ and $R_{\mathrm{meas}}^{\mathrm{calib}}(\rho)$ are the simulated and measured reflectance, respectively, of the calibration phantom. This scaling factor was then used to convert the measured reflectance data into absolute unit.

2.4.3 *Inversion procedure*

Optical properties extraction was done by searching the best fit between MC-based modeled reflectance and measured data. Reflectance intensities near and far from the source are separated by several orders of magnitude. Consequently, data transformation is necessary to balance the contributions of short and large SDS to fit accuracy.[25] The following cost function was found suitable:

$$\hat{E}(\mu_a, \mu_s') = \sqrt{\sum_{\rho} [R_{\mathrm{th}}(\mu_a, \mu_s', \rho) - R_{\mathrm{meas}}(\mu_a, \mu_s', \rho)]^2 / R_{\mathrm{meas}}(\mu_a, \mu_s', \rho)}. \tag{4}$$

The properties of the calibration phantom were chosen as initial parameters for the fitting procedure. Linear interpolation of the LUT in the μ_a, μ_s, and ρ dimensions was employed. Note that only SDS lower than 4 mm were considered in order to ensure minimal SNR.

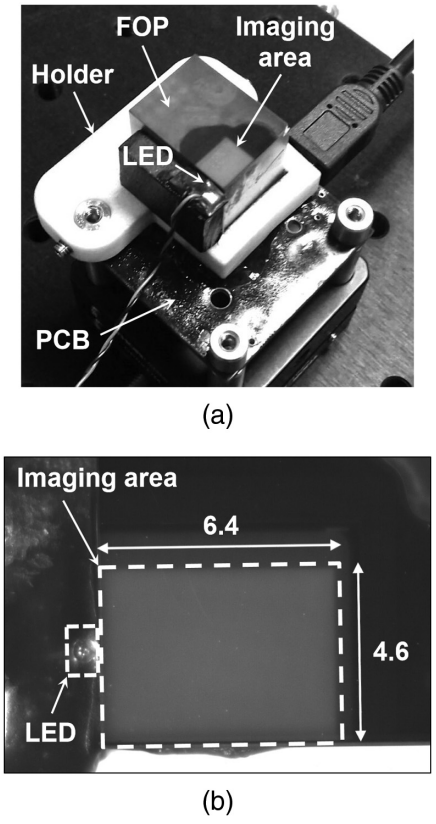

Fig. 4 Photographs of the developed prototype CMOS-based contact imaging system: (a) whole system. Note that silicon treatment was performed on the printed circuit board for isolation and impermeability of the exposed electronic parts. (b) Top view of the illumination and imaging area. Dimensions are displayed in millimeters. The CMOS sensitive area delimited by the white dotted line is viewed through the fiber optic plate.

3 Results

A prototype CMOS-based srDRS device was fabricated according to the proposed architecture (see Fig. 2). Photographs of the system are provided in Fig. 4.

The system linearity and stability of the illumination were characterized. The maximum drift from a linear behavior was smaller than 0.6% of sensor dynamic up to 80% of saturation limit. Pixel values higher than this threshold were disregarded in our processing algorithm. The illumination power out of the LED was 240 μW. Over the 1.5 h -acquisition period of LED stability measurement, the measured power did not drift by more than 0.2% from the nominal value.

As expected, fast decrease of SNR was observed as the radial distance to the source increased. Therefore, acquisition with multiple exposure times was necessary to maintain a sufficient SNR over several millimeters. The SNR was measured on the least favorable phantom (see Sec. 2.3.2) as a function of distance to the source. Using three to five exposure times separated by a factor close to 10 enabled to achieve SNR ranging from 20 to 35 dB up to 4 mm away from the illumination center.

Repeated measurements were used to evaluate the flat-field inhomogeneity (see Sec. 2.3.2). Depending on source–detector separation, the standard deviation between pixels on the same ring for a given measurement after inhomogeneity correction ranged from 3% to 5% of the mean signal. In comparison, the

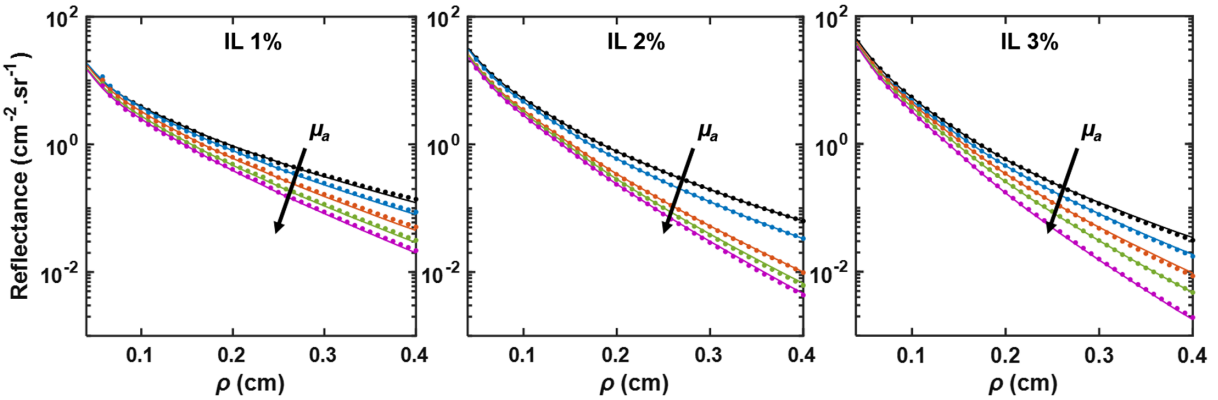

Fig. 5 Measured calibrated reflectance of Intralipid phantoms (dots) are plotted against best fits of theoretical reflectance (solid lines). Measured and fitted data for a given phantom are displayed in the same color. For clarity, only one in five points is plotted for the measured data. Each window shows measured and fitted data for a group of phantoms with same Intralipid concentration and varying ink concentration.

standard deviation between signals from different measurements at the same pixel ranged from 1.5% to 5% of the mean value.

Measured reflectance profiles versus best fits of modeled reflectance are shown in Fig. 5. The imaging area was divided into 211 rings, providing as many points on the reflectance profiles. For clarity, only one in five points is shown for the measured data in the radial dimension. Overall, measured data were well described by our forward model. Mean discrepancies between measured and modeled profiles calculated over all SDS were lower than 6.0%, 2.9%, and 3.2% for IL1%, IL2%, and IL3%, respectively.

Extracted versus expected μ_a and μ_s' of phantoms are shown in Fig. 6. Expected properties were derived from spectrophotometer measurements and Mie theory, as described in

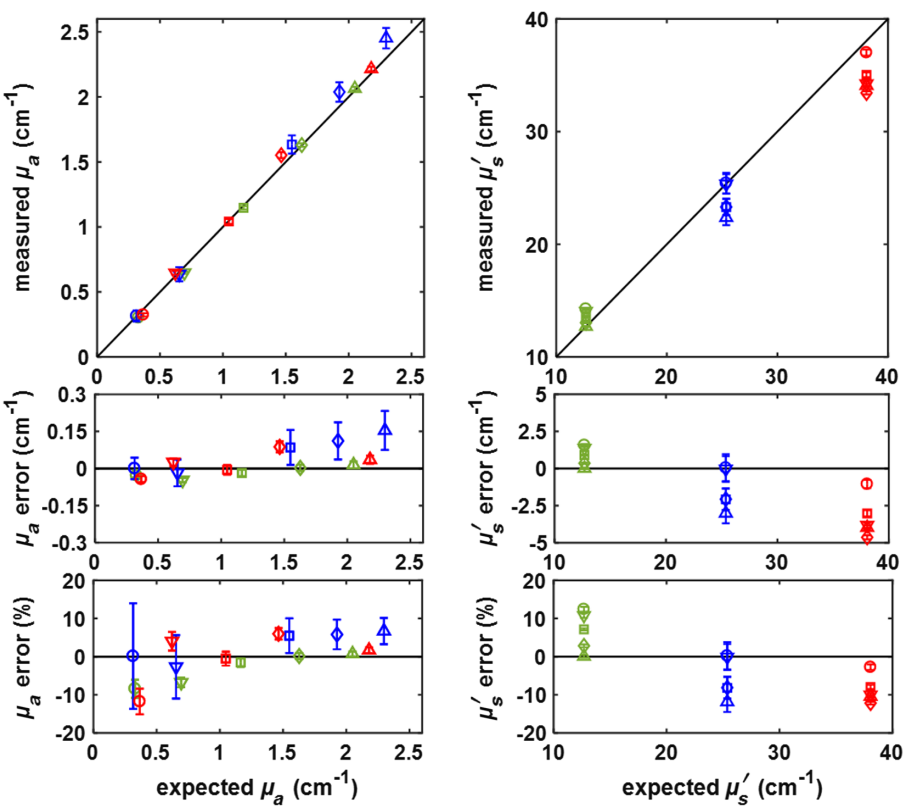

Fig. 6 Results of phantom experiments: measured optical properties for IL1% (green), IL2% (blue), and IL3% (red) are plotted against expected values (black solid line). For each Intralipid concentration, different levels of absorption are associated to different markers (from lowest to highest ink concentration: circles, downward-pointing triangles, squares, diamonds, and upward-pointing triangles). Absolute values (top), absolute errors (middle), and relative errors (bottom) between measured and expected properties are shown for (a) absorption coefficients μ_a and (b) reduced scattering coefficients μ_s'. Error bars correspond to standard deviations between measurements.

Sec. 2.3.1, and used as reference values in error calculations. Note that we did not consider error propagation in the calculation of absolute error bars, herein corresponding to the standard deviation between properties extracted from different measurements of the same phantom. Errors were calculated both in absolute value and in percent of the expected value for the considered property and phantom. Error bars for percent errors correspond to the error bars for absolute errors expressed in percent of the expected value. To estimate the overall percent error for optical properties, we considered the percent errors (in absolute value) over the whole phantom set and calculated the average. Corresponding intervals were computed as the standard deviation between percent errors (in absolute value) for different phantoms. Optical parameters were accurately measured, with overall errors of $4.2 \pm 3.5\%$ for μ_a and $7.0 \pm 4.6\%$ for μ_s'. A correlation coefficient of 0.9915 was calculated between expected and measured values. Figure 6(b) shows slight underestimation of reduced scattering coefficients for highly scattering phantoms. The calculated correlation coefficient was 0.9473. For a fixed Intralipid concentration and varying μ_a, minor variations of μ_s' estimates were observed, with standard deviations of 4.9%, 5.7%, and 4.0%, respectively for IL1%, IL2%, and IL3%. We observed that errors in measured μ_s' were closely related to the absorption level of phantoms. For all Intralipid concentrations, extracted μ_s' decreased while μ_a increased. This suggests that separation of absorption and scattering influence on measured data was not complete, and some cross-talk remained between parameters.

4 Discussion

The results obtained from phantom experiments demonstrate the ability of the developed system for accurate quantification of absorption properties of phantoms over the whole range of addressed μ_a. However, Fig. 6(b) indicates that accuracy in μ_s' extraction was correlated with the optical properties of measured phantoms. In particular, systematic underestimation of μ_s' was observed for highly scattering phantom. Additionally, the impact of absorption level of phantoms on μ_s' estimates was not completely removed, resulting in slight variations of extracted μ_s' between weakly and highly absorbing phantoms containing the same amount of Intralipid (less than 10% overall). These errors were likely due to imperfections of our instrument calibration method. The scaling factor derived in Sec. 2.4.2 solely corrects from constant multiplicative effects of the instrument response and does not include influence of the sensor optical transfer function. Furthermore, calibration could only be efficient upon precise knowledge of the source geometry. However, immersion of the srDRS system in Intralipid solutions made accurate characterization of the source profile difficult. In our forward model, a planar interface was assumed between the medium and its environment, photons being emitted from the source at this interface. In MC simulations, this interface was placed at the limit between the FOP face and phantoms. Such description was inconsistent with the actual structure of our system. Notably, the presence of the LED dome lens, possible reflections on the FOP side, and photon trajectories between the LED chip and the planar interface were not modeled. The use of phantoms fabricated in a solid material such as poly(dimethylsiloxane)[37] may facilitate the measurement and modeling of the source intensity profile.

It must be noted that the contribution from dependent scattering was not considered in our study. Several authors stressed that the effect of dependent scattering should be accounted for when high concentrations of scatterers are used.[38,39] In the reported studies, neglecting this phenomenon typically resulted in higher μ_s' expectations for a given Intralipid concentration, which might explain the observed underestimation of μ_s' compared to expected values in our case.

Because of the limitations listed before, the developed system might show inability to address a wider range of properties (currently from 0.31 to 2.30 cm^{-1} in absorption and 12.7 to 38.1 cm^{-1} in reduced scattering). In this case, use of multiple calibration phantoms, as investigated in previous studies,[29,40] could extend the accessible μ_s' range. In future work, evaluation of the device's performance on an extended range of optical properties, notably toward lower levels of absorption, should be conducted.

A major challenge in current srDRS technology is the analysis of layered tissue with specificity in depth. In skin, epithelium and stroma are the most significant structures. The separate characterization of these layers may yield critical criteria in a variety of contexts including cancer detection,[20,21] tissue oxygenation monitoring,[3] and drug permeation follow-up.[9] Epithelium thickness varies from 100 to 300 μm, depending on phenotype and location on the body.[41] Therefore, the access to both short SDS and high resolution of detection is necessary for accurate characterization of epithelial and stromal layers. Depth-resolution is directly related to lateral resolution and therefore dependent on the apparatus used for collection and detection of photons.

We demonstrated that a multipixel sensor used in contact with tissue provided possibility to image diffuse reflectance profiles with high spatial resolution and large FOV (~20 mm^2). Moreover, the developed srDRS coupling system provided a way to access short SDS in contact with an unmodified commercial CMOS sensor. In the current version of the system, however, presence of the protective glass lid induced blurring of the diffuse reflectance. Influence of this effect was studied through forward model calculations and only small impact was observed on obtained reflectance profiles. Differences between reflectance profiles affected or not by blurring were lower than 10% on the SDS range considered in our study. However, blurring of the diffuse reflectance may limit the ability of the system for the analysis of layered media such as skin, which require sensitivity to optical properties on reduced footprints. In this case, removal of the CMOS glass lid and positioning of the FOP directly on the pixel area may be investigated.[42] Moreover, validation of the system on skin-mimicking multilayer phantoms should be conducted. In order to further increase the sensitivity of diffuse reflectance spectra to superficial layers, several authors have explored the use of oblique illumination.[4,43] The proposed architecture is suitable for implementation of such approach.

5 Conclusion

A compact design for implementation of srDRS in contact with tissue has been proposed and evaluated. A prototype instrument, involving an LED source and a commercially available, unmodified CMOS sensor was fabricated. For validation of our approach, a proof-of-concept study was conducted on optical phantoms with controlled properties. Diffuse reflectance imaging was performed with high spatial resolution, large field-of-view (~20 mm^2), and SNR comparable to that of previously developed instruments.[14,18] A dedicated coupling system involving a FOP was developed to provide access to source–detector

separations as short as 480 μm. Absorption coefficients (μ_a) and reduced scattering coefficients (μ_s') of phantoms were determined with 4.2% and 7.0% error, respectively, demonstrating the ability of the system for accurate quantification of tissue optical properties. Our approach is promising for the analysis of layered media such as skin and paves the way for the development of low-cost, wearable devices for skin condition diagnosis *in vivo*.

Disclosures

The authors have no relevant financial interests in this article and no potential conflicts of interest to disclose. Nils Petitdidier and Anne Koenig are coinventors of a patent devoted to the srDRS system architecture presented in this manuscript. All rights on this patent are owned by the Commissariat à l'Energie Atomique et aux Energies Alternatives (CEA).

Acknowledgments

This work was supported by the Commissariat à l'Energie Atomique et aux Energies Alternatives (CEA).

References

1. B. Hallacoglu et al., "Absolute measurement of cerebral optical coefficients, hemoglobin concentration and oxygen saturation in old and young adults with near-infrared spectroscopy," *J. Biomed. Opt.* **17**, 081406 (2012).
2. S. Gioux et al., "First-in-human pilot study of a spatial frequency domain oxygenation imaging system," *J. Biomed. Opt.* **16**, 086015 (2011).
3. R. B. Saager et al., "In vivo isolation of the effects of melanin from underlying hemodynamics across skin types using spatial frequency domain spectroscopy," *J. Biomed. Opt.* **21**(5), 57001 (2016).
4. A. Garcia-Uribe et al., "In-vivo characterization of optical properties of pigmented skin lesions including melanoma using oblique incidence diffuse reflectance spectrometry," *J. Biomed. Opt.* **16**(2), 20501 (2011).
5. N. Rajaram et al., "Design and validation of a clinical instrument for spectral diagnosis of cutaneous malignancy," *Appl. Opt.* **49**, 142–152 (2010).
6. B. J. Tromberg et al., "Assessing the future of diffuse optical imaging technologies for breast cancer management," *Med. Phys.* **35**, 2443–2451 (2008).
7. G. Zonios et al., "Diffuse reflectance spectroscopy of human adenomatous colon polyps in vivo," *Appl. Opt.* **38**, 6628–6637 (1999).
8. L. L. Randeberg et al., "In vivo spectroscopy of jaundiced newborn skin reveals more than a bilirubin index," *Acta Paediatr.* **94**, 65–71 (2005).
9. U. Sunar et al., "Light-triggered doxorubicin release quantified by spatial frequency domain imaging and diffuse optical spectroscopy," in *Cancer Imaging and Therapy*, p. JW4A-3 (2016).
10. A. Mazhar et al., "Spatial frequency domain imaging of port wine stain biochemical composition in response to laser therapy: a pilot study," *Lasers Surg. Med.* **44**, 611–621 (2012).
11. V. Venugopalan, J. S. You, and B. J. Tromberg, "Radiative transport in the diffusion approximation: an extension for highly absorbing media and small source-detector separations," *Phys. Rev. E* **58**, 2395–2407 (1998).
12. T. Y. Tseng et al., "Quantification of the optical properties of two-layered turbid media by simultaneously analyzing the spectral and spatial information of steady-state diffuse reflectance spectroscopy," *Biomed. Opt. Express* **2**, 901–914 (2011).
13. F. Foschum, M. Jäger, and A. Kienle, "Fully automated spatially resolved reflectance spectrometer for the determination of the absorption and scattering in turbid media," *Rev. Sci. Instrum.* **82**, 103104 (2011).
14. O. Senlik and N. M. Jokerst, "Concentric multipixel silicon photodiode array probes for spatially resolved diffuse reflectance spectroscopy," *IEEE J. Sel. Top. Quantum Electron.* **22**, 7–12 (2016).
15. A. Kim et al., "A fiberoptic reflectance probe with multiple source-collector separations to increase the dynamic range of derived tissue optical absorption and scattering coefficients," *Opt. Express* **18**, 5580–5594 (2010).
16. A. Koenig et al., "Diffuse reflectance spectroscopy: a clinical study of tuberculin skin tests reading," *Proc. SPIE* **8592**, 85920S (2013)
17. A. Kim et al., "Quantification of in vivo fluorescence decoupled from the effects of tissue optical properties using fiber-optic spectroscopy measurements," *J. Biomed. Opt.* **15**(6), 067006 (2010).
18. B. Yu, H. L. Fu, and N. Ramanujam, "Instrument independent diffuse reflectance spectroscopy," *J. Biomed. Opt.* **16**(1), 11010 (2011).
19. S. Dhar et al., "A diffuse reflectance spectral imaging system for tumor margin assessment using custom annular photodiode arrays," *Biomed. Opt. Express* **3**, 3211–3222 (2012).
20. K. Terstappen et al., "Poor correlation between spectrophotometric intracutaneous analysis and histopathology in melanoma and non-melanoma lesions," *J. Biomed. Opt.* **18**(6), 061223 (2013).
21. V. T.-C. Chang et al., "Quantitative physiology of the precancerous cervix in vivo through optical spectroscopy," *Neoplasia* **11**, 325–332 (2009).
22. A. K. Mudraboyina et al., "A novel lensless miniature contact imaging system for monitoring calcium changes in live neurons," *IEEE Photonics J.* **6**, 1–15 (2014).
23. I. Schelkanova et al., "Diffuse reflectance measurements using lensless CMOS imaging chip," *J. Phys. Conf. Ser.* **541**, 012098 (2014).
24. I. Schelkanova et al., "Spatially resolved, diffuse reflectance imaging for subsurface pattern visualization toward development of a lensless imaging platform: phantom experiments," *J. Biomed. Opt.* **21**(1), 015004 (2016).
25. H. Cen, R. Lu, and K. Dolan, "Optimization of inverse algorithm for estimating the optical properties of biological materials using spatially-resolved diffuse reflectance," *Inverse Prob. Sci. Eng.* **18**, 853–872 (2010).
26. SZPHOTON Inc., "Fiber optic plate," http://szphoton.com/products/fiber-optic-plate/ (2017).
27. H. S. Cho et al., "Development of a portable digital radiographic system based on FOP-coupled CMOS image sensor and its performance evaluation," *IEEE Trans. Nucl. Sci.* **52**, 1766–1772 (2005).
28. W. Bishara et al., "Lensfree on-chip microscopy over a wide field-of-view using pixel super-resolution," *Opt. Express* **18**, 11181–11191 (2010).
29. V. Sorgato et al., "ACA-Pro: calibration protocol for quantitative diffuse reflectance spectroscopy. Validation on contact and noncontact probe- and CCD-based systems," *J. Biomed. Opt.* **21**(6), 65003 (2016).
30. H. J. van Staveren et al., "Light scattering in Intralipid-10% in the wavelength range of 400–1100 nm," *Appl. Opt.* **30**, 4507–4514 (1991).
31. S. L. Jacques, "Optical properties of biological tissues: a review," *Phys. Med. Biol.* **58**, R37 (2013).
32. T. Lister, P. A. Wright, and P. H. Chappell, "Optical properties of human skin," *J. Biomed. Opt.* **17**(9), 090901 (2012).
33. N. Bodenschatz et al., "Surface layering properties of Intralipid phantoms," *Phys. Med. Biol.* **60**, 1171–1183 (2015).
34. Q. Liu and N. Ramanujam, "Scaling method for fast Monte Carlo simulation of diffuse reflectance spectra from multilayered turbid media," *J. Opt. Soc. Am. A* **24**, 1011–1025 (2007).
35. L. G. Henyey and J. L. Greenstein, "Diffuse radiation in the galaxy," *Astrophys. J.* **93**, 70–83 (1941).
36. J. E. Bender et al., "Noninvasive monitoring of tissue hemoglobin using UV-VIS diffuse reflectance spectroscopy: a pilot study," *Opt. Express* **17**(26), 23396–23409 (2009).
37. G. J. Greening et al., "Characterization of thin poly(dimethylsiloxane)-based tissue-simulating phantoms with tunable reduced scattering and absorption coefficients at visible and near-infrared wavelengths," *J. Biomed. Opt.* **19**(11), 115002 (2014).
38. B. Aernouts et al., "Dependent scattering in Intralipid® phantoms in the 600–1850 nm range," *Opt. Express* **22**, 6086–6098 (2014).
39. G. Zaccanti, S. D. Bianco, and F. Martelli, "Measurements of optical properties of high-density media," *Appl. Opt.* **42**, 4023–4030 (2003).
40. G. Zonios and A. Dimou, "Modeling diffuse reflectance from semi-infinite turbid media: application to the study of skin optical properties," *Opt. Express* **14**, 8661–8674 (2006).

41. C. R. Flach, G. J. Zhang, and R. Mendelsohn, *Emerging Raman Applications and Techniques in Biomedical and Pharmaceutical Fields*, P. Matousek and M. D. Morris, Eds., Springer Science and Business Media, New York (2010).
42. R. G. van Silfhout and A. S. Kachatkou, "Fibre-optic coupling to high-resolution CCD and CMOS image sensors," *Nucl. Instrum. Methods Phys. Res., Sect. A* **597**, 266–269 (2008).
43. K.-B. Sung and H.-H. Chen, "Enhancing the sensitivity to scattering coefficient of the epithelium in a two-layered tissue model by oblique optical fibers: Monte Carlo study," *J. Biomed. Opt.* **17**, 107003 (2012).

Nils Petitdidier graduated as an optical engineer from IOGS, Institut d'Optique Graduate School, Palaiseau, France, and received his MS degree in engineering physics from KTH, Kungliga Tekniska Högskolan, Stockholm, Sweden, in 2015. He is currently working toward his PhD in imaging physics at the Université de Strasbourg, Strasbourg, France. His research interests are focused on the development of wearable, low-cost semiconductor spectral imaging systems for skin condition diagnosis. He is a member of SPIE.

Anne Koenig graduated as an automation and computer engineer in 1986, and then joined CEA-LETI, where she got her PhD in artificial intelligence for robotics. She received an accreditation to supervise research degrees (HDR) in 2015. Until 2005, her research focused on radiographic image processing for nondestructive testing and 3-D dynamic CT, then in the field of fluorescence diffuse optical tomography. She is now involved in skin characterization by diffuse reflectance spectroscopy.

Biographies for the other authors are not available.